




RESEARCH ARTICLE OPEN ACCESS

Moving Horizon Estimation for Al-Doped ZnO Nanoparticle Synthesis: An Online UV-vis Spectroscopy Approach

Guohui Yang¹  | Marcel K vin Jiokeng Dongmo²  | Thomas Meurer²  | Hermann Nirschl¹¹Process Machines Group, MVM, Karlsruhe Institute of Technology, Karlsruhe, Germany | ²Digital Process Engineering Group, MVM, Karlsruhe Institute of Technology, Karlsruhe, Germany**Correspondence:** Guohui Yang (guohui.yang@kit.edu) | Marcel K vin Jiokeng Dongmo (marcel.jiokeng@kit.edu)**Received:** 24 April 2025 | **Revised:** 12 June 2025 | **Accepted:** 6 July 2025**Funding:** This study received funding from the Deutsche Forschungsgemeinschaft (DFG, German Research Foundation) under the priority program “SPP 2364: Autonomous processes in particle technology” (NI 414/44-1 | ME 3231/10-1 – 504545992) and support from the KIT-Publication Fund of the Karlsruhe Institute of Technology.**Keywords:** dynamic mode decomposition | moving horizon estimation | online UV-vis spectroscopy | population balance equation | sol-gel process monitor

ABSTRACT

Nanoparticles play a pivotal role in various applications, including electronics and photovoltaics. Among the diverse synthesis techniques, the sol-gel process is widely utilized for producing transparent conductive nanostructures, such as aluminum-doped zinc oxides (AZO), which serve as cost-effective alternatives to indium tin oxide (ITO) for transparent electrodes. However, achieving precise control over critical particle properties, e.g., particle size distribution (PSD) remains a major challenge due to the inherent complexity of online monitoring during synthesis. This study develops a moving horizon estimator (MHE) to dynamically predict AZO nanoparticle properties during sol-gel synthesis. The proposed approach combines online UV-vis spectroscopy with a population balance equation (PBE) model to estimate the PSD and related parameters. To reduce computational complexity, the high-dimensional PBE model is simplified using dynamic mode decomposition with control (DMDc), retaining essential dynamics while enabling real-time state estimation. The MHE-based observer optimizes the consistency between measured and estimated AZO concentrations, demonstrating accurate real-time prediction of PSD. Experimental validation shows strong agreement between the predicted PSD and offline measurements, confirming the observer's effectiveness. This approach paves the way for model predictive control, enhancing reproducibility and product quality in the synthesis of functional semiconductor nanoparticles.

1 | Introduction

Nanoparticles are extensively employed in a wide range of applications, including pharmaceuticals, optical and electronic materials, cosmetics, photovoltaic cells, batteries, and catalysts [1–7]. The increasing demand for high-performance nanomaterials necessitates the development of advanced synthesis processes

that not only enable the efficient fabrication of functional semiconductor nanomaterials but also facilitate precise control over critical properties, such as particle size distribution (PSD). Ensuring well-defined particle and material characteristics is essential in various domains, particularly in the context of enhancing the quality and efficiency of derived products, such as solar cells and sustainable electronics [8, 9]. This requirement becomes

Guohui Yang and Marcel K vin Jiokeng Dongmo contributed equally to this work.

This is an open access article under the terms of the [Creative Commons Attribution](https://creativecommons.org/licenses/by/4.0/) License, which permits use, distribution and reproduction in any medium, provided the original work is properly cited.

  2025 The Author(s). *Nano Select* published by Wiley-VCH GmbH.

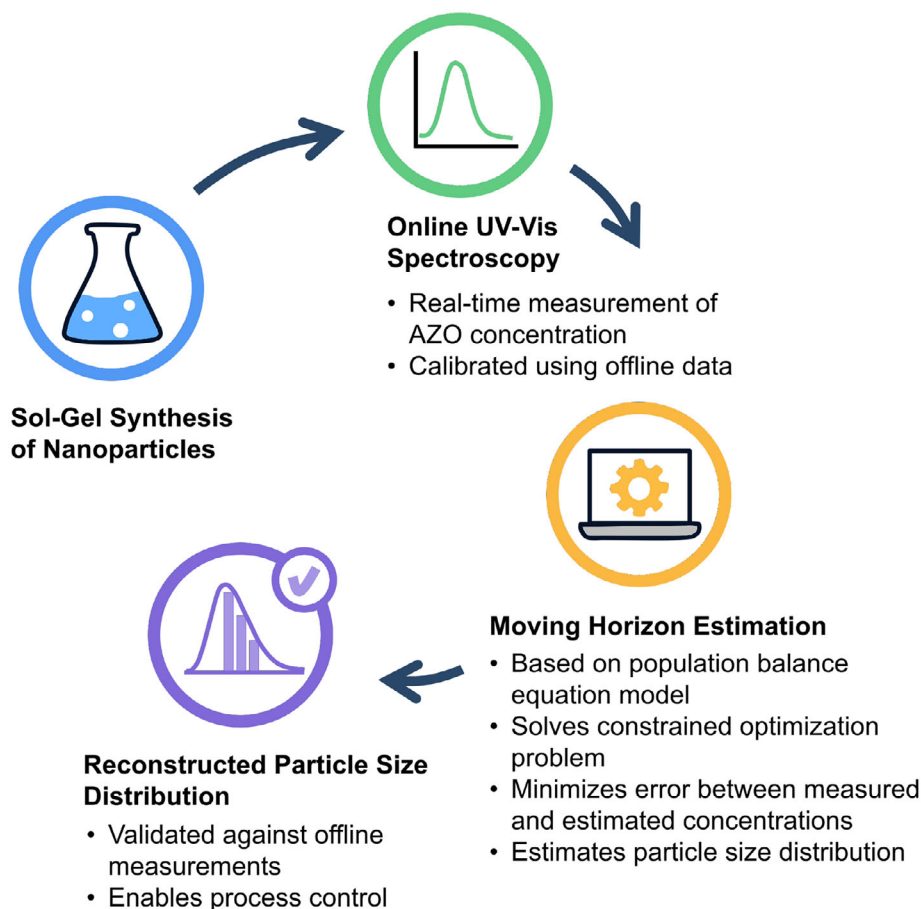


FIGURE 1 | Overview of the complete methodology, illustrating the process from online UV-vis measurements to particle size distribution reconstruction.

increasingly important in light of the global energy transition, where the rising demand for semiconductors is constrained by the limited availability of rare-earth-based materials.

Among various synthesis techniques, the sol-gel process remains the dominant approach for producing transparent conductive nanostructures via liquid-phase processes [10–14]. In the present study, the synthesis and online monitoring of aluminum-doped zinc oxide (AZO) is addressed, where zinc oxide (ZnO), a well-known wide-bandgap semiconductor, becomes a transparent conductive oxide (TCO) upon doping with trivalent ions such as Al^{3+} . As a result, AZO emerges as a cost-effective alternative to indium tin oxide (ITO) for transparent electrode applications. Gas-phase deposition techniques are known to produce high-quality crystalline thin films with resistivities comparable to ITO. However, liquid-phase synthesis offers a more economical and versatile approach, enabling various coating and printing methods, such as dip-coating, spin-coating, inkjet printing, and screen printing. Furthermore, printing-based methods eliminate the need for lithographic etching, thereby reducing material waste and enhancing process efficiency [15–17]. An additional advantage of the sol-gel synthesis route is the formation of highly crystalline AZO nanoparticles at relatively low temperatures. The inherently slow crystallization process in sol-gel synthesis facilitates time-resolved characterization, making it suitable for integrating real-time measurement technologies to monitor and control the synthesis process.

Despite the advantages of sol-gel synthesis, most studies have focused primarily on the properties of deposited sol-gel films rather than on the characteristics of the sol and colloidal particles themselves. Consequently, critical factors such as PSD and agglomeration of TCO nanoparticles have not been thoroughly investigated. Moreover, online monitoring and precise manipulation of particle properties, including PSD, number concentration (NC), and fractal dimension, remain formidable challenges due to the inherent difficulties associated with directly and rapidly measuring nanoparticle properties during synthesis. This challenge arises from the nanoscale nature of the particles and the complexity of the reaction mixture.

To address these challenges, a soft sensor approach based on a moving horizon estimator, also referred to as an observer (see, e.g., [18–20]), is developed. As depicted in Figure 1, this approach combines real-time UV-vis spectroscopy with a population balance equation (PBE) model to dynamically estimate particle properties, including PSD, during the synthesis process. The developed UV-vis spectroscopy technique introduced in Section 2 enables real-time measurement of AZO concentration in the reactor, while the PBE model is parameterized using offline measured, time-resolved particle growth data from previous studies [21–23].

A model of the synthesis process in form of a set of partial and ordinary differential equations (PDE-ODE), accounting for

subprocesses like the reaction kinetics of precursors, nucleation, growth, and aggregation of nanocrystals, is introduced to accurately track the intrinsic system states related to particle properties such as PSD, see, e.g., [24]. Due to the inherent nonlinear nature of the system, solving the PBE analytically poses significant computational challenges. Various methods have been developed to address the computational issue, including analytical solutions of PBEs [25] and discrete population balance methods [26]. To reduce computational complexity, a model order reduction technique known as dynamic mode decomposition with control (DMDc) [27] is employed, transforming the complex high-dimensional system into a simplified linear time-discrete approximation while retaining essential dynamic characteristics. The reduced-order model enables the development of a MHE, see, e.g., [28, 29] that applies to a PDE-ODE system with sensor dynamics, as demonstrated in [20]. Other observer systems applying to cell population balance models are analyzed in [30–32]. The MHE is formulated as a constrained optimization problem, minimizing the discrepancy between measured and estimated AZO concentrations to enhance real-time prediction accuracy. Similar approaches have been investigated in the context of large-scale nonlinear processes without first-principles process models [33].

By employing online UV-vis spectroscopy to measure AZO concentrations during synthesis, the soft sensor approach enables accurate PSD prediction, showing strong agreement with the offline measured PSD of the validation sample. This consistency validates the effectiveness of the proposed method in dynamically estimating PSD, facilitating real-time monitoring and control. The successful implementation of the observer facilitates the integration of modern model-based control concepts to regulate PSD, thereby enhancing reproducibility and product quality in AZO nanoparticle synthesis.

The paper is organized as follows. In Section 2, the integrated online UV-vis measurement to the closed batch reactor (CBR) is illustrated, along with calibrations to enable online determination of the AZO concentration inside the reactor. Section 3 deals with the process modeling utilizing a PBE and its parameterization through offline PSD measurements. Section 4 investigates the DMDc-based MHE technique, presenting a linear system that approximates the inherently nonlinear behavior of the PDE-ODE system. Simulation and validation results are presented in Section 5, providing empirical insights into the practical application of the proposed approach. Finally, conclusions and future outlooks are summarized in Section 6.

2 | Online UV-Vis Spectroscopy for Nanoparticle Concentration Analysis in a Closed Batch Reactor (CBR) During Sol-Gel Synthesis

Figure 2 depicts a schematic diagram of the CBR (Figure 2a) with the dilution setup (Figure 2b) and UV-vis spectroscopy (Figure 2c), allowing for the online determination of nanoparticle mass concentration. In Figure 2a, the sol-gel synthesis of AZO nanocrystals via the benzylamine (BnNH_2) route was conducted in a CBR and built upon the prior research [21–23]. The feedstock containing 25 g L⁻¹ crystalline reagents (97.5 mol% zinc acetate (Zn(acac)₂), 2.5 mol% aluminum isopropoxide ($\text{Al}(\text{OiPr})_3$),

and 250 mL aromatic solvent BnNH_2 was introduced into the CBR to synthesize AZO particles. When the reactor temperature was raised to the synthesis temperature at 110 °C, nucleation was initiated. At the end of the synthesis, the AZO concentration increased up to approximately 7 g L⁻¹, by continuously consuming the precursor Zn(acac)₂ starting from 25 g L⁻¹.

After reaching the synthesis temperature of 110 °C, the sample from reactor was semi-continuously transported using a magnetic valve (Bürkert). Due to reactor overpressure (≈ 0.8 bar), samples were rapidly transported enabling a semi-continuous gel flow. The extracted sample, containing highly concentrated precursors ($[\text{Zn}(\text{acac})_2]_{\text{max}} \approx 25$ g L⁻¹) and AZO nanoparticles ($[\text{AZO}]_{\text{max}} \approx 7$ g L⁻¹), required dilution for UV-vis measurement. A dynamic mixer integrated with an internal stirrer combined the reactor sample (≈ 0.5 mL min⁻¹) with an ethanol stream (55 mL min⁻¹) ensuring uniform dispersion. The ethanol was supplied by a peristaltic pump from the diluent reservoir. Its flowrate was measured via the flow sensor 1 in Figure 2b and maintained at 55 mL min⁻¹ by controlling the rotational speed of the peristaltic pump. The diluted sample was split before entering the flow cell, allowing a small portion to undergo measurement every 3 s while the rest was collected as waste.

The sample from the reactor mainly consisted of AZO and Zn(acac)₂, in BnNH_2 . The UV-vis spectrum reflected the superposition of AZO, Zn(acac)₂ and BnNH_2 signals, requiring calibration curves to correlate absorbance with individual component concentrations. The utilized spectrometer, featuring high resolution (0.7 nm, slit width: 10 μm) and high precision (fine wavelength increment: approximately 0.35 nm), enabled accurate peak positioning and clear differentiation of closely spaced spectral features. This combination enhanced sensitivity, data quality, and reproducibility, making it well-suited for real-time monitoring of dynamic processes and the analysis of complex mixtures. Section 2.1 details the selection of two wavelengths, 321.175 nm and 322.207 nm, chosen to minimize BnNH_2 signal and facilitate AZO concentration determination across a wide range of sizes (10–130 nm) and Al compositions (1.6–2.4 at%). For presentation simplicity in figures, the wavelength values in figure axis titles and legends are depicted in a reduced numerical format, rounded to three digits, while the precise raw wavelength values from spectrometer with six digits are provided in the corresponding captions. These calibrations (Section 2.1.2) were validated via gravimetric analysis and subsequently applied for online concentration monitoring. Furthermore, Section 2.2 establishes the relationship between reactor flow rates and the differences measured between flow sensors, enabling quantification of the dilution factor (*DF*) and calculation of AZO concentrations within the reactor (Figure 2a).

2.1 | Offline Calibration and Validation

2.1.1 | Offline Measurement and Selection of Calibration Wavelengths

The calibration experiments were conducted via offline UV-vis measurements using a series of concentration samples. To generate the concentration series, Zn(acac)₂ (BLDpharm) was diluted in ethanol to achieve concentrations up to 0.7 g L⁻¹.

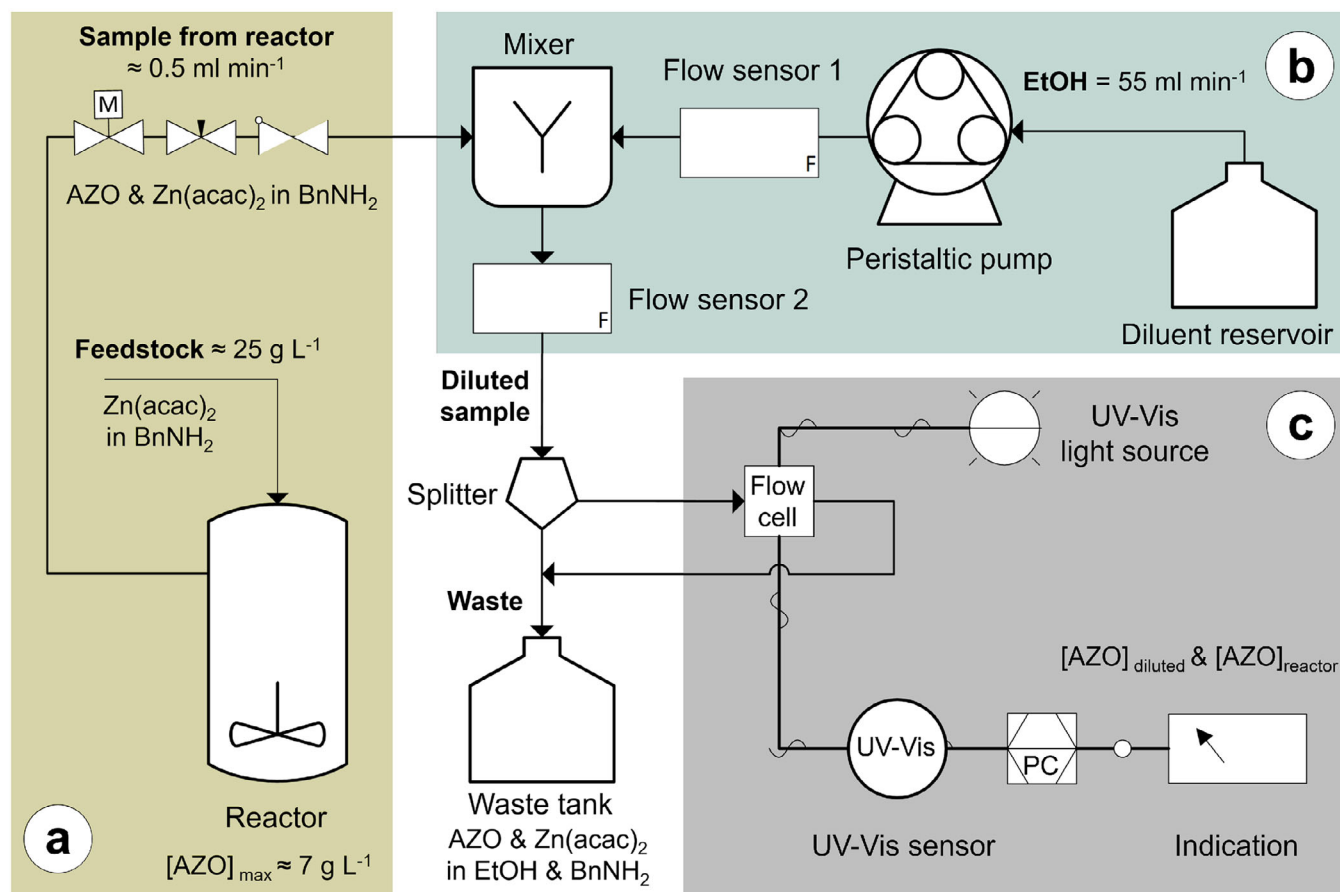


FIGURE 2 | Schematic diagram of the CBR with dilution setup and online UV-vis spectroscopy: (a) CBR with feedstock and sample stream to mixer. (b) Dilution setup necessitates a mixer (Knauer) that dilutes sample stream from reactor using ethanol transported via a peristaltic pump. (c) Online UV-vis part, constructed by a UV-vis light source (Ocean Optics, DH2000), flow cell made of Teflon (FIALab, SMA-Z cell, 10 mm optical path) and a sensor (Ocean Optics, HR6). The absorbance of the diluted sample is continuously measured inside the flow cell.

Similarly, synthesized AZO particles, following purification, were used to prepare AZO concentration series ranging from 0.01 to 0.6 g L^{-1} . Additionally, benzylamine series were prepared with volume ratios of benzylamine to ethanol varying from 0.0005 to 0.1. For each measurement, pure ethanol was used as the background. Consequently, the obtained spectra, with the background signal subtracted, represented the absorbance of the measured solutes: AZO, $\text{Zn}(\text{acac})_2$, and BnNH_2 , respectively.

Absorbance spectra were recorded over the wavelength range of 250 to 800 nm. It was observed that BnNH_2 exhibited significant absorbance only at wavelengths up to 300 nm, while beyond 300 nm, its absorbance became negligible compared to that of AZO and $\text{Zn}(\text{acac})_2$. This characteristic, as illustrated in Figure 5, simplifies the analysis of reactor samples after dilution by reducing the signal interpretation from a ternary to a binary system, considering only AZO and $\text{Zn}(\text{acac})_2$ contributions at wavelengths above 300 nm.

To select suitable calibration wavelengths for AZO samples with varying doping levels, the spectral differences between AZO and pure ZnO were investigated. AZO exhibits a blue-shifted absorption edge (350–370 nm) compared to ZnO (375–390 nm), resulting in lower absorbance in the visible range (400–700 nm) and, consequently, enhanced transparency. However, in the UV region

(<400 nm), both ZnO and AZO display a pronounced absorption edge, functioning as effective UV absorbers, particularly in the UV-B region (280–315 nm), where their absorption characteristics are highly comparable.

Figure 3 illustrates the impact of the blue-shifted absorption edge. As shown in Figure 3a, at the wavelength of 322.207 nm (near the UV-B region), a consistent correlation between AZO absorbance and concentration was observed, regardless of variations in aluminum composition (1.6–2.4 at% as determined by EDX mapping) and particle size (10–130 nm). In contrast, at the wavelength 400.119 nm (Figure 3b), near the visible range, the absorbance correlation differed significantly due to varying levels of Al doping. Specifically, AZO samples with 2.4 at% aluminum exhibit lower absorbance compared to those with 1.6 at% aluminum, demonstrating that higher aluminum doping increased transparency in the visible range. Furthermore, similar doping- and size-independent correlations between AZO absorbance and concentration were consistently observed for other wavelengths between 300 and 322 nm. It confirmed the feasibility of selecting the wavelengths from 300 to 322 nm to construct AZO's calibration curves.

Figure 4 presents the correlation between AZO and $\text{Zn}(\text{acac})_2$ concentrations at wavelengths exceeding 300 nm, specifically

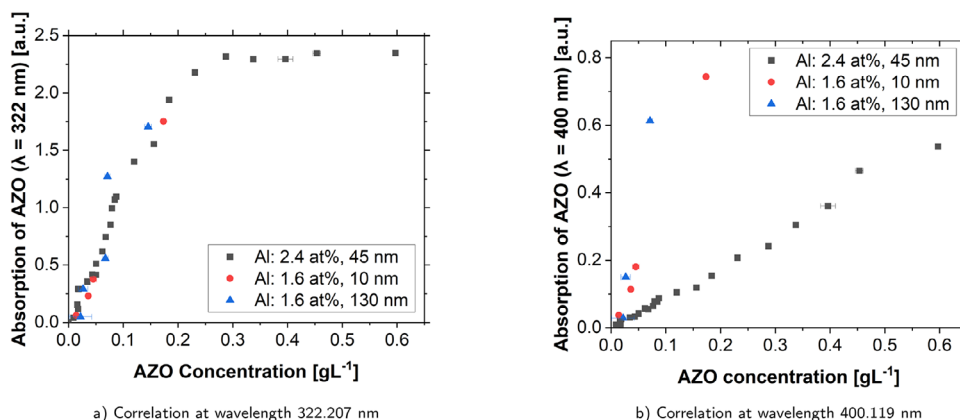


FIGURE 3 | UV-vis correlation curves for AZO nanocrystals of different sizes and doping level: (a) at wavelength 322.207 nm. (b) at wavelength 400.119 nm.

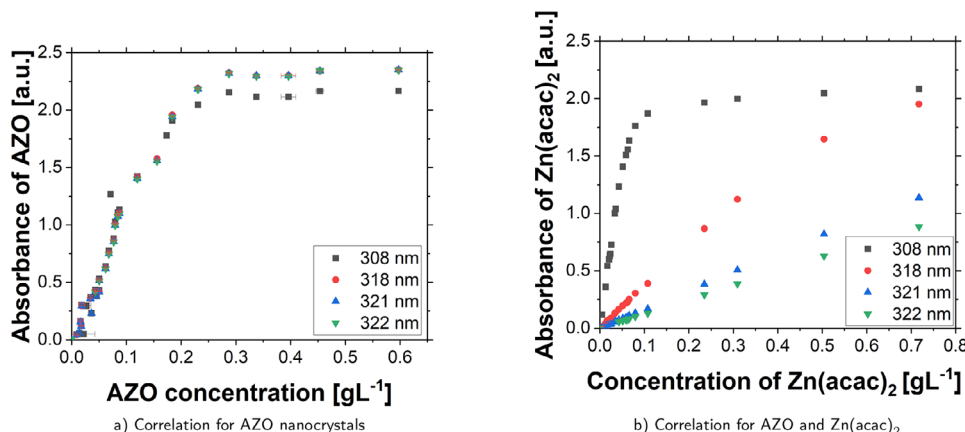


FIGURE 4 | Correlation for AZO nanocrystals and precursor $\text{Zn}(\text{acac})_2$ at wavelengths beyond 300 nm, in and near UV-B range: 308.088, 318.078, 321.175, and 322.207 nm: (a) AZO's correlation. (b) $\text{Zn}(\text{acac})_2$'s correlation.

308.088, 318.078, 321.175, and 322.207 nm. As shown in Figure 4a, the absorbance trend of AZO among these wavelengths exhibited a high degree of similarity within the linear range, up to an absorbance of approximately 1.2, in accordance with the Beer–Lambert law. Beyond this threshold, the exponential increase observed in three of the correlations demonstrated comparable behavior, with stabilization occurring at a concentration of approximately 0.3 g L^{-1} . The correlation at 308.088 nm, however, deviated from this pattern. At concentrations exceeding 0.2 g L^{-1} , it exhibited noticeably lower absorbance compared to the other wavelengths. In contrast, the remaining three wavelengths above 308.088 nm demonstrated advantageous characteristics, as their absorbance stabilized slightly later, providing an extended and more precise correlation.

Figure 4b illustrates the differences in the absorbance of $\text{Zn}(\text{acac})_2$ at various wavelengths within the concentration range up to 0.7 g L^{-1} . Significant differences were observed in the correlation of $\text{Zn}(\text{acac})_2$ across the investigated wavelengths. At 321.175 and 322.207 nm, the absorbance fully obeyed the Beer–Lambert law, demonstrating a clear linear relationship throughout the entire concentration range. In contrast, at lower wavelengths (308.088 and 318.078 nm), the absorbance was markedly higher and exhibited a combined linear and expo-

ponential rise. This deviation from the Beer–Lambert law was particularly pronounced at 308.088 nm, where the linear relationship was restricted to concentrations below 0.1 g L^{-1} . Beyond this concentration, the absorbance stabilized, indicating that accurate concentration determination without sample dilution is feasible only up to 0.1 g L^{-1} at 308.088 nm. Consequently, for higher concentrations ($> 0.1 \text{ g L}^{-1}$), the precision of concentration calculation is considerably limited. In contrast, the higher wavelengths (321.175 and 322.207 nm) maintained a linear correlation up to 0.7 g L^{-1} , fully conforming to the Beer–Lambert law. This extended linear range significantly improves the accuracy of AZO concentration determination, especially in more concentrated samples.

The key criteria for selecting and optimizing the calibration wavelengths (321.175 and 322.207 nm) for accurate determination of AZO and $\text{Zn}(\text{acac})_2$ concentrations in the reaction mixture are summarized below.

1. Select wavelengths beyond 300 nm to eliminate the absorbance of BnNH_2 , reducing the complexity from a tertiary system (AZO , $\text{Zn}(\text{acac})_2$, BnNH_2) to a binary system (AZO and $\text{Zn}(\text{acac})_2$).

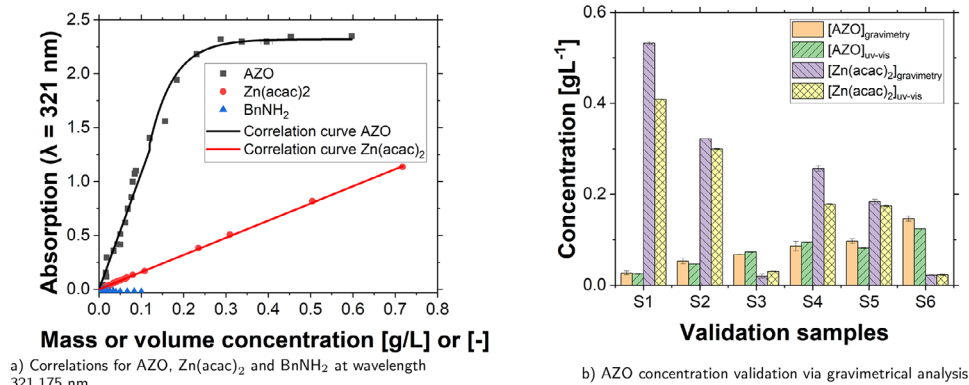


FIGURE 5 | (a) UV-vis correlations between absorbance and mass/volume concentrations in ethanol, including AZO mass concentration, Zn(acac)₂ mass concentration, and BnNH₂ volume concentration at the selected calibration wavelength of 321.175 nm. (b) Validation of the calibration relationships presented in Table 1 by comparing UV-vis-derived concentrations with those obtained through gravimetric analysis.

- Prioritize wavelengths in the UV range, particularly near UV-B region (280–315 nm), due to the blue-shifted absorption edge of AZO.
- Choose wavelengths that ensure an extended linear correlation for accurate concentration determination. In the UV-B region, for instance, the wavelength of 308.088 nm fails to determine Zn(acac)₂ concentrations beyond 0.1 g L⁻¹ without dilution. In contrast, wavelengths of 321.175 and 322.207 nm maintain a linear correlation up to 0.7 g L⁻¹, enabling precise measurements even for concentrated samples.

2.1.2 | Construction and Validation of Calibration Curves

As described in Section 2.1.1, two calibration wavelengths were selected beyond 300 nm and near the UV-B range: 321.175 and 322.207 nm. Figure 5a depicts the absorbance for the tertiary system at the wavelength 321.175 nm. As previously explained, the absorbance of BnNH₂ was negligible at both wavelengths. The absorbance of AZO remained consistent at both wavelengths, enabling precise determination of AZO concentration up to 0.3 g L⁻¹ without the need for sample dilution. Additionally, the absorbance of Zn(acac)₂ increased almost linearly with concentration up to 0.7 g L⁻¹, maintaining accuracy without requiring dilution.

The offline measurements for varying AZO and Zn(acac)₂ concentrations were fitted using the following piecewise equation (Equation 1) to establish calibration equations for the simplified binary system.

$$y = \begin{cases} ax, & \text{for } x \leq x_c \\ b(1 - e^{-c(x-d)}), & \text{for } x > x_c \end{cases} \quad (1)$$

The upper linear correlation ax in Equation (1) has been utilized to parametrize the low concentration range in Figure 5a. This correlation quantifies the linear increase in absorbance concerning the rising concentration up to a critical concentration x_c , where absorbance reached approximately 1.2. In this range, the data followed the Beer-Lambert law. However, when the

TABLE 1 | Calibrated parameters for piecewise calibration equations, including a , b , c , and d in Equations (2.1) and (2.2) for AZO and Zn(acac)₂ at the selected calibration wavelengths 321.175 and 322.207 nm.

Calibrated wavelengths	Binary system	a	b	c	d
$\lambda_1 = 321.175$ nm	AZO	11.56	2.32	17.46	0.07
	Zn(acac) ₂	1.593	NA	NA	NA
$\lambda_2 = 322.207$ nm	AZO	11.56	2.32	17.46	0.07
	Zn(acac) ₂	1.236	NA	NA	NA

concentration exceeded x_c and the absorbance surpassed 1.2, the increase in absorbance became relatively slower, exhibiting an exponential trend. Consequently, the lower equation part $b(1 - e^{-c(x-d)})$ has been applied to describe the exponential growth at higher concentrations. The calibrated parameters a , b , c , and d are listed in Table 1, and exemplary parameterized correlation curves are shown in Figure 5a, demonstrating consistent fits with the measured data points.

At wavelengths 321.175 and 322.207 nm, the AZO calibration equations contain both linear and exponential components. The correlations of absorbance to concentration are identical, sharing the same calibrated parameters a , b , c , and d , as presented in Table 1. In contrast, the Zn(acac)₂ calibration curves consist solely of the linear part, with the slope at 321.175 nm being higher than that at 322.207 nm. The observed difference in absorbance between wavelengths 321.175 nm and 322.207 nm for Zn(acac)₂ is reasonable, given the high-resolution spectrometer (0.7 nm resolution and 0.35 nm increment) and the characteristics of the absorption spectra. For Zn(acac)₂, both wavelengths lay on the right slope of a narrow absorption peak, where the absorbance decreased sharply. Consequently, even a minor wavelength shift resulted in variations in absorbance. Notably, a concentration increment of 0.1 g L⁻¹ led to an absorbance variation of approximately 0.036 at both wavelengths. In contrast, AZO nanoparticles exhibited broader and more gradual absorption features, resulting in nearly identical absorbance at 321.175 and 322.207 nm. This difference between Zn(acac)₂ and AZO is attributed to the

distinct spectral characteristics of each compound. The narrow, steep peak of $\text{Zn}(\text{acac})_2$ rendered it highly sensitive to small wavelength changes, whereas the broader peak of AZO ensured more consistent absorbance across similar wavelengths.

The calibration functions at wavelength 321.175 and 322.207 nm, quantify the total absorbance of samples consisting AZO and $\text{Zn}(\text{acac})_2$ in BnNH_2 . The absorbance of BnNH_2 is negligible and thereby the total absorbance is attributed to addition of AZO and $\text{Zn}(\text{acac})_2$. The $\text{Abs}_{321.175}$ and $\text{Abs}_{322.207}$ in both Equation (2.1) and Equation (2.2) refer to the measured absorbance via UV-vis for samples containing AZO, $\text{Zn}(\text{acac})_2$ and BnNH_2 . The unknown concentrations for AZO and $\text{Zn}(\text{acac})_2$ are denoted as $[\text{AZO}]$ and $[\text{Zn}(\text{acac})_2]$, which are obtained by solving following equations by measuring $\text{Abs}_{321.175}$ and $\text{Abs}_{322.207}$ such that

$$\begin{aligned} \text{Abs}_{321.175} &= 1.593[\text{Zn}(\text{acac})_2] \\ &+ \begin{cases} 11.56[\text{AZO}], & 0 < [\text{AZO}] \leq 0.12 \\ 2.32(1 - e^{-17.46([\text{AZO}] - 0.07)}), & 0.12 < [\text{AZO}] \leq 0.6 \end{cases} \end{aligned} \quad (2.1)$$

and

$$\begin{aligned} \text{Abs}_{322.207} &= 1.236[\text{Zn}(\text{acac})_2] \\ &+ \begin{cases} 11.56[\text{AZO}], & 0 < [\text{AZO}] \leq 0.12 \\ 2.32(1 - e^{-17.46([\text{AZO}] - 0.07)}), & 0.12 < [\text{AZO}] \leq 0.6, \end{cases} \end{aligned} \quad (2.2)$$

where $[\text{Zn}(\text{acac})_2] \in (0, 0.7)$.

Multiple samples containing AZO and $\text{Zn}(\text{acac})_2$ at varying concentrations were prepared using the gravimetric method and analyzed using the developed UV-vis correlation. The AZO concentrations calculated using the calibrated equations (Equations 2.1 and 2.2) were consistent with the gravimetric results (Figure 5b) and these correlations were subsequently employed for real-time concentration monitoring.

2.2 | CBR With Dilution Setup and Online UV-Vis Spectroscopy

2.2.1 | Determination of Dilution Factor

For online UV-vis spectroscopy, directly measuring reactor samples was impractical due to their high concentrations ($[\text{Zn}(\text{acac})_2]_{\text{max}} \approx 25 \text{ g L}^{-1}$, $[\text{AZO}]_{\text{max}} \approx 7 \text{ g L}^{-1}$). Therefore, as previously mentioned, it is necessary to dilute the reactor samples prior to measurements. Consequently, the sample measured in the flow cell (see Figure 2c) corresponded to the diluted one, and the calculated concentrations were based on these diluted samples. To obtain real-time AZO concentrations inside the reactor (for undiluted samples), the concentration correlation between the undiluted samples ($[\text{AZO}]_r$) in the reactor and the diluted samples ($[\text{AZO}]_d$) in the flow sensor 2 after mixing was established via the mass balance equation for AZOs ($\dot{m}_r = \dot{m}_{fs2}$).

Additionally, a dilution factor is introduced to account for the dilution effect.

$$[\text{AZO}]_r \dot{V}_r = [\text{AZO}]_d \dot{V}_{fs2} \quad (2.3a)$$

$$[\text{AZO}]_r = \frac{\dot{V}_{fs2}}{\dot{V}_r} [\text{AZO}]_d \quad (2.3b)$$

with a defined dilution factor

$$DF = \frac{\dot{V}_{fs2}}{\dot{V}_r} \quad (2.3c)$$

2.2.2 | Correlation Between Reactor Flowrates and Flowmeter Signals

As depicted by Equation (2.3b) and Equation (2.3c), the dilution factor is required to calculate the AZO concentration inside the reactor ($[\text{AZO}]_r$) based on the measured diluted AZO concentration ($[\text{AZO}]_d$) in the flow cell. The numerator, \dot{V}_{fs2} , in Equation (2.3c) was continuously recorded by the flow sensor 2. However, the denominator, \dot{V}_r , represents the reactor sample flow rate and was influenced by flow rate difference measured by both flow sensors. A simple subtraction of the flow rates recorded by flow sensor 2 and flow sensor 1 did not yield an accurate \dot{V}_r due to the effects of excess volume when mixing liquids. To address this, a calibration was performed to correlate the reactor sample flow rates with the difference in flow sensor signals. This relationship is illustrated in Figure 6b, with the detailed calibration equation provided in Figure S2.

Since the online samples consisted of AZO and residual precursors in BnNH_2 , it is reasonable to assume that they exhibit identical excess volume behavior to their solvent, BnNH_2 . Therefore, pure BnNH_2 (Sigma-Aldrich) was used to construct the correlation. The needle valve along the sampling line in Figure 2a was adjusted to generate varying BnNH_2 flow rates from the reactor. Ethanol was supplied at a constant flow rate of 55 mL min^{-1} . After dilution, the BnNH_2 samples were measured online in the flow cell to record UV-vis spectra of diluted BnNH_2 .

As described in Section 2.1.1, UV-vis calibration was performed for BnNH_2 . At a wavelength of 287.022 nm, the correlation between absorbance and the volume ratio of BnNH_2 to ethanol was established, as depicted in Figure 6a. Using this calibration (refer to the calibration equation in Figure S1), the recorded spectra were analyzed to determine the benzylamine-to-ethanol volume ratio and the BnNH_2 flow rates from the reactor. Reactor flow rates of up to 1.6 mL min^{-1} were calibrated against flow rate differences measured by the flow sensors, which ranged up to 1.2 mL min^{-1} . Dilution of BnNH_2 with ethanol resulted in a total volume reduction. As a result, during the synthesis, the flowrates from reactor (\dot{V}_r) were calculated according to the linear relationship based on the signal difference of flow sensors. This further enabled quantification of dilution factor, to calculate the AZO concentration ($[\text{AZO}]_r$) inside reactor.

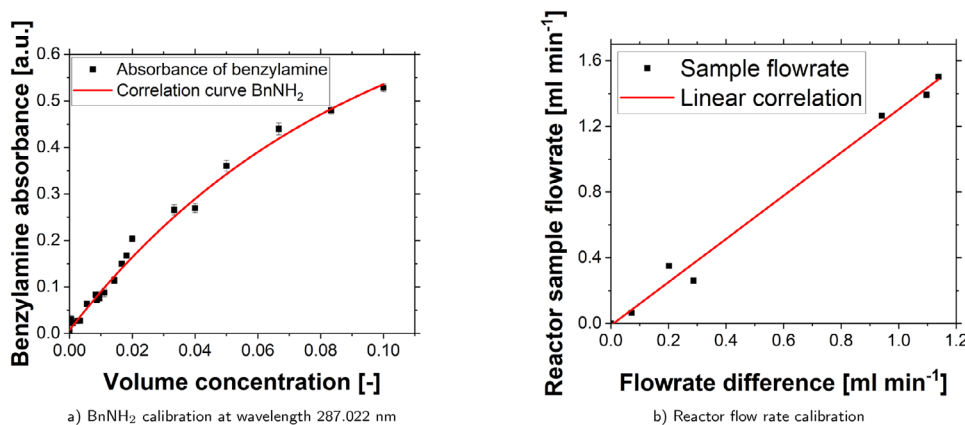


FIGURE 6 | Determination of sample flowrates from reactor according to the differences between flow sensors: (a) UV-vis correlation curve of BnNH₂ at the wavelength of 287.022 nm, illustrating an exponential elevate of absorbance with increasing the volume ratio of BnNH₂ to ethanol. (b) Established correlation to quantify the reactor sample flow rates based on the differences between flow sensors 2 and 1 in Figure 2b.

2.2.3 | Online Calculation of Nanoparticle Concentration in CBR

The developed online UV-vis technique was applied to the sol-gel synthesis to monitor the AZO nanocrystal concentration in reactor using the implemented calibrations, including

1. Calibration equations for AZO and Zn(acac)₂ at wavelengths 321.175 and 322.207 nm. These UV-vis correlations enable the determination of AZO concentration in the diluted reactor samples ([AZO]_d) measured in the flow cell.
2. Calibrated correlations between reactor flow rates and flow rate differences measured by the flow sensors. These correlations facilitated the accurate quantification of the dilution factor.

By continuously determining the diluted AZO concentration ([AZO]_d) through online UV-vis measurements and calculating the dilution factor based on the difference between flow sensors 2 and 1, the real-time AZO concentration ([AZO]_r) was continuously quantified (Figure 9a). These data were simultaneously used to reconstruct real-time particle states (details in Section 5).

2.3 | Validation of PSD via Transmission Electron Microscopy (TEM)

To further assess the performance and accuracy of the implemented MHE-based observer, diluted samples were extracted online for validation purposes. The extracted samples primarily consisted of AZO, Zn(acac)₂ and BnNH₂ in ethanol. AZO crystals were purified by centrifugation to remove impurities. During purification, BnNH₂ and residual Zn(acac)₂ were dissolved in ethanol and subsequently eliminated through centrifugation, leaving the undissolved AZO particles. The purified AZO nanoparticles were then dispersed in ethanol and air-dried on a TEM grid at 25°C. TEM imaging was performed to visualize the particles on the grid. Using ImageJ, 300 nanoparticles were counted to obtain the PSD of the AZO particles. This approach enabled a direct comparison between the real-time PSD obtained

from TEM analysis and the reconstructed PSD generated by the soft sensor (see Section 5).

3 | Process Modeling and Parameter Identification

A synthesis process model is presented using a combination of partial and ordinary differential equations, capturing key subprocesses such as reaction kinetics, nucleation, growth, and nanocrystal aggregation, in order to precisely monitor intrinsic system states linked to particle characteristics like PSD. Using offline measurements of crystal mass concentration and particle NC, the first principle model is parameterized. It enables the PSD reconstruction based on the AZO mass concentration. The objective is to develop a model-based approach for online estimating the AZO mass concentration and reconstructing the PSD using online UV-vis measurements (refer to Section 2).

3.1 | Mathematical Model

A widely accepted approach for modeling particle synthesis processes using PDEs involves the application of a PBE. The PBE describes the evolution of the PSD and particle number density. To capture the complete system behavior, it is coupled with the reaction kinetics of the precursor, zinc acetylacetonate (Zn(acac)₂). For simplicity, the concentration of Zn(acac)₂ is denoted as [Zn] throughout this section. Together, these elements govern the overall system dynamics.

$$\begin{aligned} \partial_t [\text{Zn}](t) &= -k(T)[\text{Zn}](t), \quad t > 0 \\ \partial_t n(x, t) &= -G([\text{Zn}])\partial_x n(x, t) + B([\text{Zn}], x) \\ &\quad - P_{\text{agg}}([\text{Zn}], x)n(x, t), \quad x \in (0, x_{\text{max}}), \quad t > 0 \end{aligned} \quad (3.1a)$$

with boundary conditions

$$n(0, t) = 0, \quad t > 0, \quad (3.1b)$$

and initial conditions

$$n(x, 0) = n_0(x), \quad [\text{Zn}](0) = [\text{Zn}]_0, \quad x \in [0, x_{\max}]. \quad (3.1c)$$

Herein, $[\text{Zn}](t)$ denotes the zinc precursor concentration and $n(x, t)$ the particle number density of monocrystals with diameter x . The PBE is composed of three main parts: the growth term $G([\text{Zn}])\partial_x n(x, t)$, the nucleation term $B([\text{Zn}], x)$ and the aggregation term $P_{\text{agg}}([\text{Zn}], x)n(x, t)$ defined as

$$\begin{aligned} B([\text{Zn}], x) &= k_{\text{nuc}}k(T)[\text{Zn}]^b\phi(x, \mu_{\text{mono}}) \\ G([\text{Zn}]) &= k_gk(T)[\text{Zn}]^g \\ P_{\text{agg}}([\text{Zn}], x) &= k_{\text{agg}}k(T)[\text{Zn}]^aP(x, \mu_{\text{agg}}), \end{aligned} \quad (3.2)$$

where $\phi(x, \mu_{\text{mono}})$ denotes a normal distribution function with mean μ_{mono} and $P(x, \mu_{\text{agg}})$ is the probability that particles with size x aggregate at μ_{agg} . The birth and aggregation terms are assumed continuous in x , continuously differentiable in t and locally Lipschitz continuous in $n(x, t)$ uniformly in t on bounded intervals. This implies the existence and the uniqueness of a mild solution of (3.1), see, e.g., [34, Thm. 6.1.4].

The model parameters are summarized in the vector $\mathbf{p} = [\mu_{\text{mono}}, \mu_{\text{agg}}, b, g, a, k_{\text{nuc}}, k_g, k_{\text{agg}}]^T$ and will be determined by making use of the offline measurement data. The quantity $k(T)$ represents the rate constant and it is modeled using the Arrhenius law, see also [23]. The output of the system is defined as

$$\partial_t \nu(x_m, t) = P_{\text{agg}}([\text{Zn}], x)n(x, t), \quad (3.3)$$

where $\nu(x_m, t)$ is the number density of mesocrystals with size $x_m \in [0, x_{\max}]$. The estimation process of [AZO] utilizing a moving horizon estimation (MHE) approach is conducted as elaborated in ref. [35]. To determine [AZO](t), the third moment of (3.3) is exploited, which is given by

$$M_3(t) = \int_0^{x_{\max}} x^3 \nu(x, t) dx. \quad (3.4)$$

The total particle number is obtained by exploiting the zeroth moment of (3.3), which is given by

$$M_0(t) = N(t) = \int_0^{x_{\max}} \nu(x, t) dx. \quad (3.5)$$

The [AZO](t) of mesocrystals follows as

$$[\text{AZO}](t) = y(t) = \frac{M_{\text{AZO}}}{N_{\text{avo}}v_{\text{AZO}}}M_3(t) \quad (3.6)$$

with N_{avo} the Avogadro number, M_{AZO} the molecular mass, $M_3(t)$ as well as v_{AZO} the third moment of the PBE and unit volume of an AZO monocrystal, respectively. The [AZO] is assumed to be measured and employed for reconstructing the PSD, enabling the estimation of the optimal initial state of (3.1), which will be used to calculate the particle size defined as

$$d_v(t) = \left(\frac{6}{\pi} \frac{M_3(t)}{M_0(t)} \right)^{\frac{1}{3}} = \left(\frac{6}{\pi} \frac{N_{\text{avo}}v_{\text{AZO}}}{M_{\text{AZO}}M_0(t)} y(t) \right)^{\frac{1}{3}}, \quad t > 0, \quad (3.7)$$

see, e.g., [36]. The temperature $T(t)$ in the reactor is assumed homogeneous and is introduced into the model using

$$\tau \partial_t T(t) = -T(t) + Q(t), \quad 0 \leq Q(t) \leq Q_{\max}, \quad (3.8)$$

where τ represents a time constant, $Q(t)$ is the control input and refers to the energy generated by heating cartridges. A subordinate PI control is implemented to guide the process so that a quick temperature response $T(t)$ is achieved, considering the bounded control $Q(t)$. The particle synthesis occurs in two distinct steps: the preheating phase of the process is conducted at 50 °C, while the synthesis phase is carried out at a temperature of 110 °C.

3.2 | Semi-Discrete Model

To numerically solve the PDE-ODE system (3.1), a discretization approach using backward finite differences is employed on the PDE part of the system. This results in a finite dimensional approximation consisting of a set of ODEs. Here, the spatial coordinate x is discretized using a uniform grid of q nodes $x_i = i\Delta x$, $i \in \{1, \dots, q\}$ for $\Delta x = \frac{x_{\max}}{q-1}$. Let $\mathbf{n}_i(t) \equiv \mathbf{n}(x_i, t)$ so that $\mathbf{n}(t) = [n_1(t), \dots, n_q(t)]^T$ and consider backward finite differences to approximate the first order derivative

$$\partial_x n(x_i, t) \approx \frac{n_i(t) - n_{i-1}(t)}{\Delta x}.$$

The system Equation (3.1) then evaluates to

$$\begin{aligned} \partial_t n_i(t) &= -G \frac{n_i(t) - n_{i-1}(t)}{\Delta x} + b_i - P_{\text{agg},i} n_i(t) \\ &= -\left(\frac{G}{\Delta x} + P_{\text{agg},i} \right) n_i(t) + \frac{G}{\Delta x} n_{i-1}(t) + b_i \\ &= R_i n_i(t) + \frac{G}{\Delta x} n_{i-1}(t) + b_i, \end{aligned} \quad (3.9)$$

where $b_i = b([\text{Zn}], x_i)$, $G = G([\text{Zn}])$, $P_{\text{agg},i} = P_{\text{agg}}([\text{Zn}], x_i)$, $R_i = -(G/\Delta x + P_{\text{agg},i})$ and $n_0 = 0$, whereby the ODE for $[\text{Zn}](t)$ is left aside for sake of clarity.

Equation (3.9) results in a set of linear ODEs with respect to $\mathbf{n}(t)$ and reads

$$\partial_t \mathbf{n}(t) = \mathbf{A} \mathbf{n}(t) + \mathbf{b}, \quad (3.10)$$

where

$$\mathbf{A} = \begin{bmatrix} R_1 & 0 & \dots & 0 & 0 \\ \frac{G}{\Delta x} & R_2 & \dots & 0 & 0 \\ \vdots & \vdots & \ddots & \vdots & \vdots \\ 0 & 0 & \ddots & R_{q-1} & 0 \\ 0 & 0 & \dots & \frac{G}{\Delta x} & R_q \end{bmatrix}$$

and $\mathbf{b} = [b_1, \dots, b_q]^T$. The resulting system can thus be defined as

$$\dot{\mathbf{X}}(t) = \frac{d}{dt} \begin{bmatrix} [\text{Zn}] \\ \mathbf{n}(t) \\ T(t) \end{bmatrix} = \begin{bmatrix} -k(T)[\text{Zn}] \\ A\mathbf{n}(t) + \mathbf{b} \\ -\frac{T(t)}{\tau} + Q(t) \end{bmatrix}, \quad t > 0 \quad (3.11a)$$

$$\mathbf{X}(0) = \mathbf{X}_0, \quad (3.11b)$$

where $\mathbf{X}(t) = [[\text{Zn}](t), \mathbf{n}(t), T(t)]^T \in \mathbb{R}^{q+2}$. The number density of mesocrystals is obtained as

$$\dot{\mathbf{v}}(t) = \mathbf{P}_{\text{agg}}([\text{Zn}]) \odot \mathbf{n}(t), \quad t > 0, \quad (3.12)$$

where $\mathbf{P}_{\text{agg}}([\text{Zn}]) = [P_{\text{agg},1}, \dots, P_{\text{agg},q}]^T$, $\mathbf{v}(t)$ represents the spatially discretized number density of the mesocrystals and \odot introduces the element-wise vector multiplication. The model parameters are identified by solving a static optimization problem that minimizes the error between the offline measured data and the first-principles model. This optimization yields the parameter set \mathbf{p} as $\mu_{\text{mono}} = 23$ nm, $\mu_{\text{agg}} = 58$ nm, $b = 5.29$, $g = 9.19$, $a = 0.85$, $k_{\text{nuc}} = 10^{14.84}$, $k_g = 1$ and $k_{\text{agg}} = 1$, see ref. [35]. Depending on the CPU, the simulation requires at least 30 s of computation time, even with a relatively coarse spatial discretization. Refining the discretization for smoother state representations significantly increases the simulation time, rendering (3.11) unsuitable for real-time applications.

In the following section, the parameterized model is utilized to design a linear time-discrete model, which facilitates online particle mass concentration estimation. The implementation of the MHE (see Section 4) relies on a well-calibrated measurement unit, as discussed in Section 2. The determined AZO concentration measured by online UV-vis is utilized by the MHE in estimating the optimal particle states, e.g., PSD, ensuring accurate particle concentration predictions at each iteration.

4 | DMDc and Moving Horizon Estimation

The objective of this section is to develop a moving horizon estimator (MHE) based on the DMDc model derived from the introduced PDE-ODE system. This approach enables the real-time state estimation and reconstruction during the synthesis process (Algorithms 1 and 2).

4.1 | DMDc

A time-discrete linear approximation of (3.11) is achieved using the Koopman operator based approach, specially DMDc. For this, the full DMDc algorithm is introduced, see, e.g., [27, 35, 37]. To achieve this, snapshots \mathbf{X}_1 , \mathbf{X}_2 and \mathbf{Y} of (3.11) are gathered at regular time intervals $\Delta t = \frac{T_{\text{sim}}}{m}$ that capture state and input behavior

$$\begin{aligned} \mathbf{X}_1 &= [\mathbf{X}(t_0) \mathbf{X}(t_1) \dots \mathbf{X}(t_{m-1})] \\ \mathbf{X}_2 &= [\mathbf{X}(t_1) \mathbf{X}(t_2) \dots \mathbf{X}(t_m)] \\ \mathbf{Y} &= [Q(t_0) Q(t_1) \dots Q(t_{m-1})] \end{aligned} \quad (4.1)$$

ALGORITHM 1 | Dynamic mode decomposition with control

- 1: **Input:** State snapshots \mathbf{X}_1 , future states \mathbf{X}_2 , inputs \mathbf{Y}
- 2: **Output:** System matrix \bar{A} and input vector \bar{b} such that $\mathbf{x}_{j+1} \approx \bar{A}\mathbf{x}_j + \bar{b}Q_j$
- 3: Concatenate state \mathbf{X}_1 and input \mathbf{Y} data matrices: $\mathbf{\Omega} = \begin{bmatrix} \mathbf{X}_1 \\ \mathbf{Y} \end{bmatrix}$
- 4: Compute least-squares fit: $[\bar{A} \quad \bar{b}] = \mathbf{X}_2 \cdot \mathbf{\Omega}^\dagger$
 $\mathbf{\Omega}^\dagger$ represents the Moor–Penrose pseudo-inverse of $\mathbf{\Omega}$
- 5: Low-rank approximation:
 - Perform SVD: $\mathbf{\Omega} = \mathbf{U}_\Omega \mathbf{\Sigma}_\Omega \mathbf{V}_\Omega^*$
 - Truncate to rank r : keep first r singular values
 - Use truncated $\mathbf{\Omega}_r^\dagger$ to improve robustness: $\mathbf{\Omega}_r = \mathbf{U}_r \mathbf{\Sigma}_r \mathbf{V}_r^*$
- 6: **Output:** $[\bar{A} \quad \bar{b}] = \mathbf{X}_2 \mathbf{V}_r \mathbf{\Sigma}_r^{-1} \mathbf{U}_r^* = \mathbf{X}_2 \mathbf{V}_r \mathbf{\Sigma}_r^{-1} [\mathbf{U}_{r,1}^* \quad \mathbf{U}_{r,2}^*]$

ALGORITHM 2 | Moving horizon estimation pseudo-code

- 1: **Input:** Initial state estimate $\hat{\mathbf{x}}_0$, horizon length θ , model estimation $\hat{\mathbf{y}}_k$, measurements y_k , control inputs Q_k
- 2: **for** each time step k **do**
- 3: Collect measurements $y_{k-\theta:k-1}$ and inputs $Q_{k-\theta-1:k-2}$
- 4: Solve (4.7) to obtain estimated states $\hat{\mathbf{x}}_{k-\theta:k-1}$
- 5: Set $\hat{\mathbf{x}}_k$ as the current state estimate
- 6: **end for**
- 7: **Output:** Estimated state $\hat{\mathbf{x}}_k$

such that

$$\mathbf{X}_2 = \bar{A}\mathbf{X}_1 + \bar{b}\mathbf{Y} = [\bar{A} \quad \bar{b}] \begin{bmatrix} \mathbf{X}_1 \\ \mathbf{Y} \end{bmatrix}, \quad \mathbf{X}_2 \approx \mathbf{G}\mathbf{\Omega}, \quad (4.2)$$

where the optimal $\mathbf{G} = [\bar{A} \quad \bar{b}]$ is calculated by minimizing the residual in terms of Frobenius norm $\|\mathbf{X}_2 - \mathbf{G}\mathbf{\Omega}\|_f$ and T_{sim} represents the simulation time. This leads to the time discrete model

$$\mathbf{x}_{j+1} = \bar{A}\mathbf{x}_j + \bar{b}Q_j, \quad (4.3)$$

where $\bar{A} \in \mathbb{R}^{q+2 \times q+2}$, $\bar{b} \in \mathbb{R}^{q+2}$, $\mathbf{x}_j = [[\text{Zn}]_j, \mathbf{n}_j, T_j]^T \in \mathbb{R}^{q+2}$, $[\text{Zn}]_j \in \mathbb{R}$, $\mathbf{n}_j \in \mathbb{R}^q$, $T_j \in \mathbb{R}$, $Q_j \in \mathbb{R}$, for $j \in \{0, 1, \dots, m\}$ with m representing the number of snapshots needed to compute the DMDc-based model. In this context, $\mathbf{x}_j = \mathbf{x}(t_j)$, where t_j represents evenly spaced sampling points. The objective of this method is to efficiently determine the matrix \bar{A} and the input vector \bar{b} , effectively capturing the dominant system dynamics by utilizing snapshots of the parameterized nonlinear model derived from offline measurement data. This process is completed by performing a singular value decomposition (SVD) on the input subspace $\mathbf{\Omega}$. The reduced left singular matrix \mathbf{U}_Ω obtained is then utilized to project the state into its original space. A truncation of the system to rank $r = 10$ is performed to retain the first dominant singular values of the SVD, which contain the majority of the system's information, see [35] for a detailed introduction of the simulation-based MHE for the underlying system. Initially, these offline data are utilized to parameterize (3.11), which is then employed to extract necessary snapshots at regular time

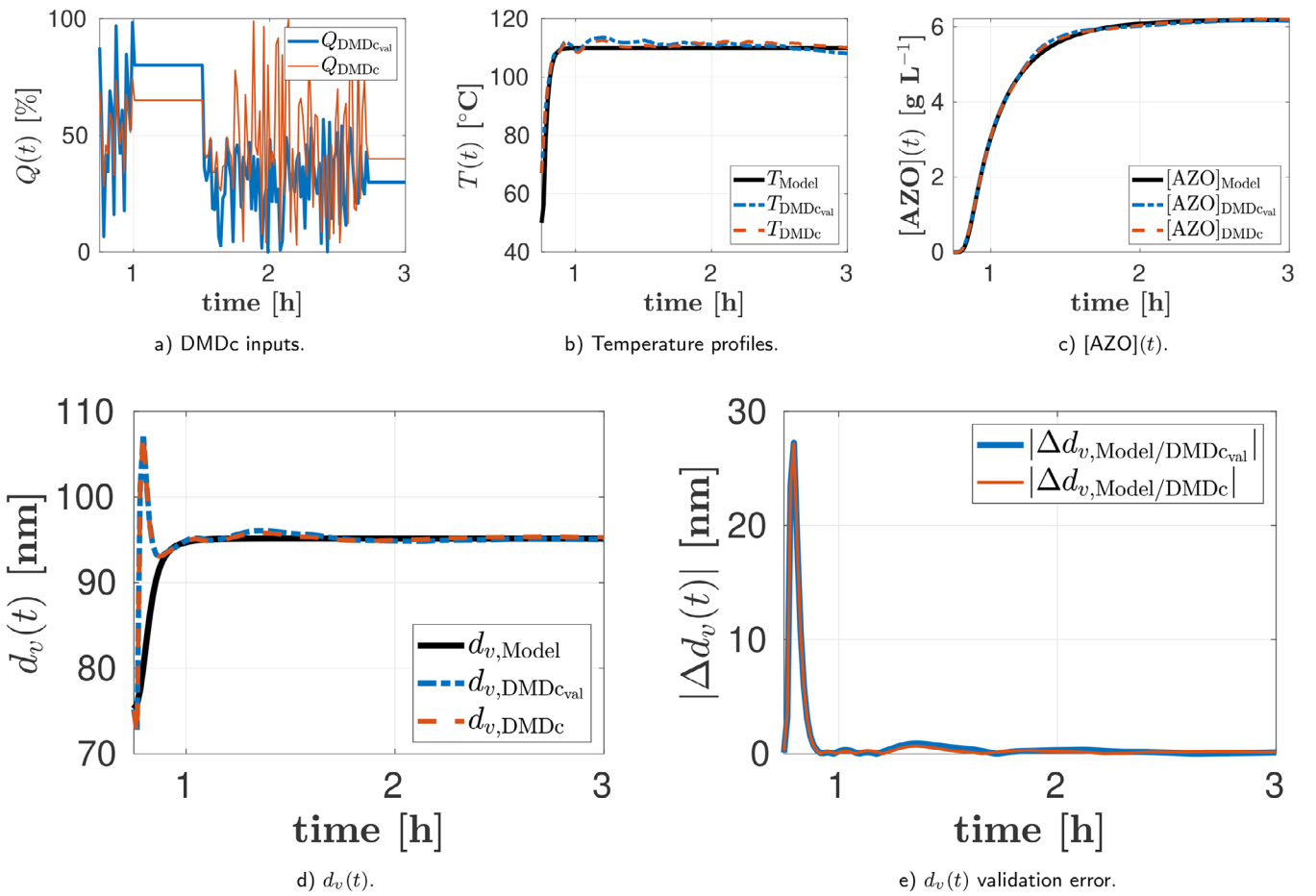


FIGURE 7 | DMDc validation: (a) represents the input power used to train (red curve) and to validate (blue curve) the DMDc Model. In (b)–(d), the black curve describes the temperature profile, [AZO], and particle size of the nonlinear model during the nominal reaction scenario, while the red and the blue curve represent their profiles obtained by the DMDc model based on training and validation data, respectively. (e) depicts the error between the full model and the trained DMDc for both input datasets.

intervals t_j . A pseudo-code to implement DMDc is introduced below (see more details in ref. [27, Sec. 3.4]).

Subsequently, the number density of the aggregates is expressed as

$$\mathbf{v}_j = \tilde{\mathbf{C}} \mathbf{x}_j \quad (4.4)$$

with the output matrix $\tilde{\mathbf{C}} \in \mathbb{R}^{q \times q+2}$ and $\mathbf{v}_j \in \mathbb{R}^q$. The discrete time AZO concentration can be rewritten as

$$[\text{AZO}]_j = y_j = \tilde{\mathbf{c}}^T \mathbf{v}_j, \quad (4.5)$$

where $\tilde{\mathbf{c}}^T \in \mathbb{R}^{1 \times q}$ is a row vector composed of (3.6) and the integral in (3.4). Note that this integral is evaluated using the trapezoidal rule. This leads to the following definition of the particle size

$$d_{v,j} = \tilde{\mathbf{\kappa}}^T \mathbf{v}_j, \quad (4.6)$$

where $\tilde{\mathbf{\kappa}}^T \in \mathbb{R}^{1 \times q}$ represents a row vector comprised of the discretized integrals as well as parameters of (3.7).

The validation of the designed DMDc-based model is illustrated in Figure 7, showcasing the relationship between input, [AZO],

NC, and particle size. The DMDc is determined for $m = 200$ snapshots and the spatial discretization of (3.9) set to $q = 400$. The input signals utilized to generate (red) and validate (blue) the time-discrete model are depicted in Figure 7a, while the corresponding resulting temperature profiles are shown in Figure 7b. Here, the black temperature curve is obtained from the parameterized model. It is evident that temperature variations directly influence concentration, size and number of particles. Moreover, particle size growth occurs rapidly, leading to a relatively uniform particle size being achieved within the initial heating minutes, as demonstrated in Figure 7d. Depending on the applied input, an acceptable approximation of the parameterized model (blue line) by the DMDc-based model is achieved, as shown in Figure 7c. The differences observed between the DMDc-based signals can be attributed to the temperature variations resulting from the input energy. The particle size error is calculated by assessing the percentage of the absolute difference between the identified model and the DMDc-based model, relative to the maximum value between $d_{v,\text{Model}}(t)$ and $d_{v,\text{DMDc}}(t)$ and $d_{v,\text{Model}}(t)$ and $d_{v,\text{DMDc}_{\text{val}}}(t)$, respectively, such that, e.g.,

$$\Delta d_{v,\text{Model/DMDc}}(t) = \frac{|d_{v,\text{Model}}(t) - d_{v,\text{DMDc}}(t)|}{\max(\max(d_{v,\text{Model}}(t)), \max(d_{v,\text{DMDc}}(t)))} \times 100.$$

During time intervals when the red input exceeds the blue input in Figure 7a, corresponding changes are observed in the temperature profile (Figure 7b), AZO concentration (Figure 7c), and particle size (Figure 7d), and the reverse is true when the blue input is larger. This demonstrates the sensitivity of the DMDc-based model to various inputs, which influence both the AZO concentration and the particle size.

4.2 | Moving Horizon Estimation

The primary objective of MHE is to minimize the error between measured and estimated AZO concentration values over a finite receding horizon θ , see, e.g., [18, 28, 38]. In this context, the focus is on reconstructing the PSD based on the parameterized system (3.11) under disturbances. To achieve this, the reduced-order model (4.3) is used to represent the system dynamics. Thus, only the measured AZO concentration y_i is used for the estimation process. Hence, the state estimation problem can be formulated as

$$\min_{\hat{\mathbf{x}}_{k-\theta}} J = \frac{\Delta t}{4} \sum_{j=k-\theta}^{k-1} [(\Delta y_{j+1})^2 + (\Delta y_j)^2] \quad (4.7a)$$

for $\Delta y_j = y_j - \hat{y}_j$ subject to

$$\hat{\mathbf{x}}_{j+1} = \bar{\mathbf{A}}\hat{\mathbf{x}}_j + \bar{\mathbf{b}}Q_j, \quad j = k - \theta, \dots, k - 1, k \in \mathbb{N}_{\geq 0} \quad (4.7b)$$

$$\hat{\mathbf{v}}_j = \bar{\mathbf{C}}\hat{\mathbf{x}}_j, \quad \hat{y}_j = \bar{\mathbf{c}}^T \hat{\mathbf{v}}_j \quad (4.7c)$$

with $\theta \in \mathbb{N}_{>0}$ denoting the horizon length and \hat{y}_j the estimation of the AZO concentration. The initial value $\hat{\mathbf{x}}_{k-\theta}$ represents the decision variable and Q_j corresponds to the input at discrete time j , respectively. The function J is approximated by making use of the trapezoidal rule. The optimization problem (4.7) is solved repeatedly on the receding finite time horizon θ to find the optimal initial state $\hat{\mathbf{x}}_{k-\theta}$ minimizing J . The MHE employs an SQP algorithm to capitalize on the linear characteristics of the DMDc model. This approach efficiently addresses a quadratic and nonlinear subproblem, ensuring smooth and locally optimal solutions through gradient-based updates. The reader is kindly referred to [20] for a detailed description of the MHE algorithm implementation, specifically tailored for a PDE-based system incorporating sensor dynamics. A pseudo-code for implementing the MHE for the underlying system is provided below (see more details in ref. [29]).

5 | Simulation and Experimental Results

The particle synthesis process lasted over a total duration of 3 h with the initial precursor concentration of 25 g L⁻¹. The initial 45 min of this time frame were dedicated to the preheating phase. During this phase, the reactor temperature was raised to 50°C for 30 min and was subsequently maintained at this level for additional 15 min. This temperature adjustment was made to optimize dispersion of the precursor species into benzylamine. It is assumed that no particles were formed during this preheating phase due to the relatively low temperature. After preheating, the

synthesis phase began. During this phase, the reactor temperature was rapidly increased to the target reaction temperature of 110°C, controlled by a subordinate PI controller. The first sample was extracted after the synthesis temperature reached 110°C, which occurred 1 h after the start of the process. Subsequent samples were taken at regular intervals of 5 min to monitor the progress of the synthesis over time. Offline measurements, including PSD and NC, on the samples with increasing synthesis time were employed for parameterizing the mathematical model, which is used to generate snapshots in the context of the DMDc, forming the foundation upon which the MHE design is based [35].

The assumption of a uniform temperature directly impacts the robustness of the nonlinear model (3.11), as nucleation and growth kinetics in particle synthesis are highly temperature-dependent. Key kinetic parameters such as reaction rate constants, solubility, and diffusivity exhibit Arrhenius-type behavior, making temperature control critical for model accuracy and predictive power. Similarly, the assumption of negligible mixing gradients is introduced to support the validity of the DMDc-based model. Incomplete mixing or the presence of concentration gradients can create localized regions with elevated precursor concentrations, promoting inhomogeneous nucleation and deviation from the well-mixed dynamics the model is built upon. This may lead to model-plant mismatch and reduce the observability of internal states such as PSD from external measurements like AZO concentration obtained via UV-vis spectroscopy. Such a mismatch can degrade estimator performance, especially under real-time state estimation frameworks using MHE. These challenges are most pronounced in large-volume systems with poor thermal coupling, high viscosity, inadequate stirrer design, or insufficient mixing intensity. In contrast, the assumptions are well-justified in the present experimental setup. The synthesis is performed in a small-scale, well-controlled batch reactor equipped with enhanced temperature regulation and mixing, achieved via an embedded PI controller and efficient stirrer configuration. The low reaction volume and high thermal coupling further minimize the spatial gradients. Therefore, the assumptions of uniform temperature and negligible concentration gradients are reasonable within this setup and provide a solid foundation for using lumped-parameter models and implementing efficient real-time estimators.

5.1 | Simulation Results for DMDc-Based MHE

The estimation time window spanned five discretization steps corresponding to $\theta = 4.5$ min. The MHE approach demonstrated the ability to accurately track measurements, and it exhibited rapid convergence of the estimation error, even in the presence of additive noise on [AZO]. The initial state, represented as $\hat{\mathbf{X}}_0 = [[\widehat{\text{Zn}}]_0, \hat{\mathbf{n}}_0(\mathbf{x}), \hat{T}_0]^T$, was deliberately set to differ from the initially measured states. Figure 8 refers to the visual representation and validation of these results. The reconstructed PSD (continuous colored lines) at sampling times is shown in Figure 8c, showcasing the ability of the MHE to track nonmeasurable states. The reader is referred to ref. [35] for more detailed results of the MHE design for the underlying system. The sensitivity analysis of the MHE is evaluated using the root mean square error (RMSE),

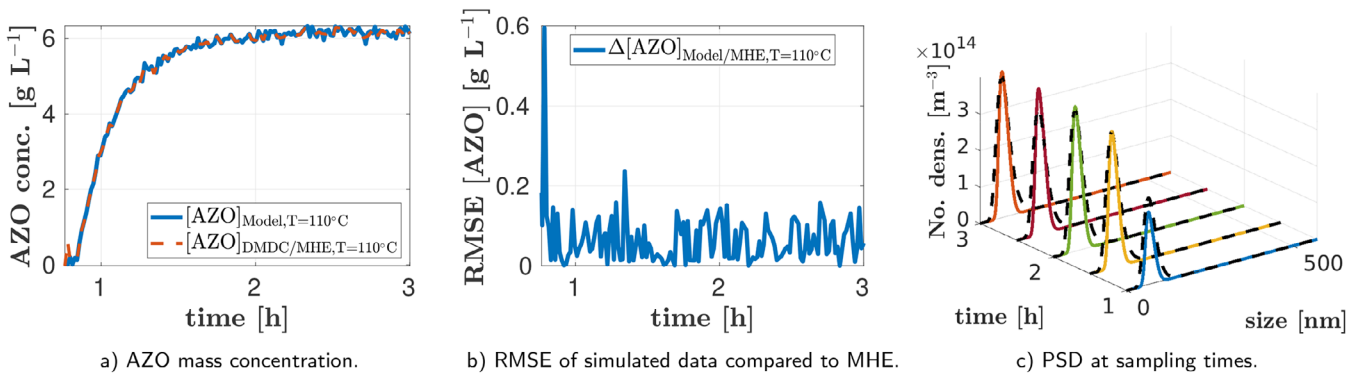


FIGURE 8 | Evaluation of DMDC-based MHE using simulation results.

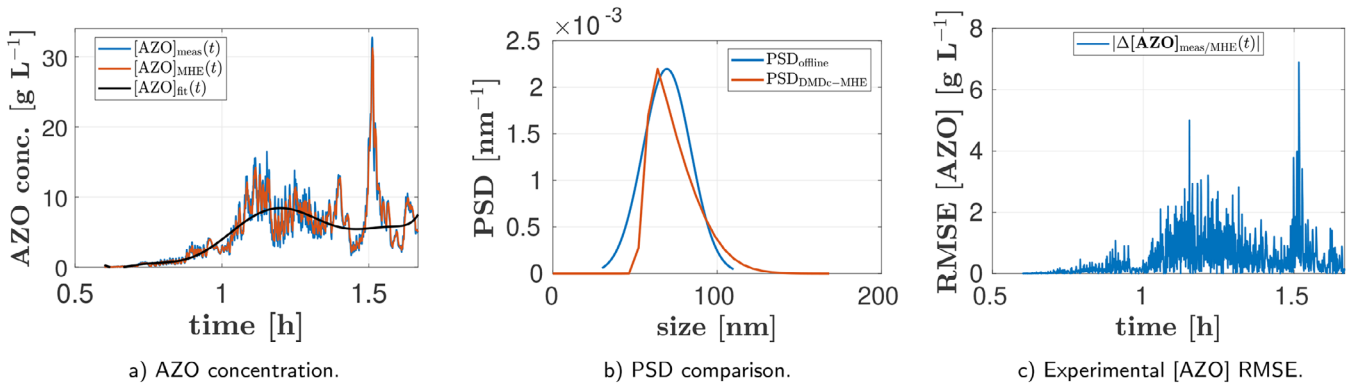


FIGURE 9 | MHE experimental results: (a) represents the measured (blue), the estimated and the polynomial fit of the AZO concentration. (b) shows the qualitative comparison of the PSD reconstructed from the by the MHE and the TEM results. Here, TEM indicates the mean AZO particle size of 69.4 nm, while the mean size of the reconstructed PSD is 74.2 nm. (c) depicts the RMSE between the measure and the estimated AZO concentration.

providing a quantitative measure of the estimation accuracy under varying conditions. It is defined as

$$\text{RMSE} = \sqrt{\frac{1}{n} \sum_{i=1}^n (y_i - \hat{y}_i)^2},$$

where y_i denotes the measured or actual value, \hat{y}_i the predicted or model value and n the number of samples. The low RMSE in Figure 8b signifies a magnitude difference between the true value (blue) and the estimation (red) in Figure 8a. A MHE-iteration step has an average computational time of 0.08s considering an Intel Core i5-8265U CPU.

5.2 | Online Experimental Results

LabVIEW was used to interface with the plant's devices, while Python handled the calibration equations, and MATLAB was employed for state estimation and reconstruction. The experiment lasted for 100 min after reaching the synthesis temperature at 110°C, during which data were recorded for subsequent processing. Every 3 s, the spectrum of the diluted reactor sample captured by the UV-vis sensor was processed using a Python-based calibration algorithm (Section 2.1.2) to determine the AZO concentration online. Throughout the experiment, the

reactor pressure was manually regulated using an needle valve to maintain the pressure in range between 0.5 and 0.8 bar, and the suspension outflow into the dilution cycle was controlled by a magnetically actuated valve with periodic openings. These measures aimed to facilitate solution extraction while minimizing abrupt volume fluctuations. However, the manual actuation of the pressure valve made it challenging to fully eliminate these fluctuations, see, e.g., Figure 9a at $t \in \{1.1, 1.3, 1.5\}$ h. Consequently, variations in reactor pressure led to increased suspension inflow into the dilution cycle, causing a rapid decrease in the dilution factor. These fluctuations directly impacted the measured AZO concentration, as shown in Figure 9a. Despite the pressure fluctuations affecting the AZO concentration profile, the DMDC-based model effectively computes the PSD for moment-based AZO concentration estimation. The red curve in Figure 9a illustrates the AZO concentration estimated using MHE. MHE successfully tracks the actual measured particle concentration in the reactor and accurately reconstructs the PSD, as shown in Figure 9b. Additionally, a polynomial fit was applied to the experimental measurements ($[\text{AZO}]_{\text{fit}}$ in Figure 9a) to characterize the average concentration behavior over the course of the process. Figure 9a illustrates the capability of the MHE to track the AZO concentration, a conclusion further validated in Figure 9b, where the PSD of a sample (blue curve) taken during synthesis was highly comparable to the PSD reconstructed (red curve) using MHE.

The modal diameter of AZO particles, measured offline via TEM, was 64.9 nm, while the MHE-predicted modal diameter was 63.8 nm. For the mean particle size, TEM indicated 69.4 nm, whereas the MHE-reconstructed PSD yielded 74.2 nm, reflecting a modest deviation of 4.8 nm. The results highlight the high approximation accuracy of the MHE, affirming its effectiveness in reconstructing PSD. To quantify the discrepancy between measured and estimated AZO concentrations throughout the experiment, the root mean square error was employed. RMSE captured the average magnitude of the deviation between sensor measurements and DMDc-based estimates. A lower RMSE reflected better alignment and thus higher estimation accuracy (see Figure 9c).

6 | Conclusions

In this study, an early-lumping MHE approach is introduced for the real-time estimation of particle concentration in view of reconstructing the PSD.

For this, a nonlinear mathematical model of the synthesis process is determined and parameterized based on offline measurement data. To obtain a real-time capable model, DMDc is conducted to achieve a linear time-discrete approximation of the nonlinear model based on snapshots of the parameterized model. To realize real-time measurements of the AZO concentration during the experiment, an online UV-vis measurement technique is developed. Here, the absorbance correlation of the major components in reaction mixture to their concentration is calibrated for online determining the AZO nanocrystal concentration within the reactor. Based on these measurements, a MHE-based soft sensor is designed and implemented to firstly estimate the nanoparticle concentration and secondly to reconstruct the PSD. The experimental results showcase the effectiveness and applicability of the approach of the UV-vis-based MHE in providing precise and real-time estimation of the AZO concentration and the related PSD. This methodology and the obtained results will serve as basis for future research aimed at actively controlling PSD as well as related product properties such as bandgap, transparency and electrical and thermal conductivity.

Acknowledgments

This study received funding from the Deutsche Forschungsgemeinschaft (DFG, German Research Foundation) under the priority program "SPP 2364: Autonomous processes in particle technology" (NI 414/44-1 | ME 3231/10-1 – 504545992) and support from the KIT-Publication Fund of the Karlsruhe Institute of Technology. The authors thank H. Störmer for support with the electron microscopy.

Open access funding enabled and organized by Projekt DEAL.

Conflicts of Interest

The authors declare no conflicts of interest.

Data Availability Statement

The data that support the findings of this study are available from the corresponding author upon reasonable request.

References

1. T. Stubhan, H. Oh, L. Pinna, J. Krantz, I. Litzov, and C. J. Brabec, "Inverted Organic Solar Cells Using a Solution Processed Aluminum-Doped Zinc Oxide Buffer Layer," *Organic Electronics* 12, no. 9 (2011): 1539–1543.
2. D. Winarski and F. Selim, "Synthesis of Conductive Sol-Gel ZnO Films and Development of ZnO Printed Electronics," in *Sol-Gel Method-Design and Synthesis of New materials With Interesting Physical, Chemical and Biological Properties* (IntechOpen, 2019), 53–74.
3. S. Qiu, K. Wu, B. Gao, L. Li, H. Jin, and Q. Li, "Solution-Processing of High-Purity Semiconducting Single-Walled Carbon Nanotubes for Electronics Devices," *Advanced Materials* 31, no. 9 (2019): 1800750.
4. W. Scheideler and V. Subramanian, "Printed Flexible and Transparent Electronics: Enhancing Low-Temperature Processed Metal Oxides With 0D and 1D Nanomaterials," *Nanotechnology* 30, no. 27 (2019): 272001.
5. I. Singh and B. I. Birajdar, "Novel tio₂ Photocatalyst Using Nonaqueous Solvent-Controlled Sol-Gel Route," in *Titanium Dioxide-Material for a Sustainable Environment* (IntechOpen, 2018).
6. K. He, G. Zhao, and G. Han, "Template-Free Synthesis of tio₂ Microspheres With Tunable Particle Size via a Non-Aqueous Sol-Gel Process," *CrystEngComm* 16, no. 34 (2014): 7881–7884.
7. N. Pinna, S. Grancharov, P. Beato, P. Bonville, M. Antonietti, and M. Niederberger, "Magnetite Nanocrystals: Nonaqueous Synthesis, Characterization, and Solubility," *Chemistry of Materials* 17, no. 11 (2005): 3044–3049.
8. L. Meng, H. Chai, X. Yang, Z. Lv, and T. Yang, "Optically Rough and Physically Flat tco Substrate Formed by Coating ZnO Thin Film on Pyramid-Patterned Glass Substrate," *Solar Energy Materials and Solar Cells* 191 (2019): 459–465.
9. S. J. Lee, S. Kim, D. C. Lim, D. H. Kim, S. Nahm, and S. H. Han, "Inverted Bulk-Heterojunction Polymer Solar Cells Using a Sputter-Deposited Al-Doped ZnO Electron Transport Layer," *Journal of Alloys and Compounds* 77 (2019): 717–722.
10. J.-H. Lee and B.-O. Park, "Transparent Conducting ZnO: Al, In and Sn Thin Films Deposited by the Sol-Gel Method," *Thin Solid Films* 426, no. 1–2 (2003): 94–99.
11. V. Musat, B. Teixeira, E. Fortunato, R. Monteiro, and P. Vilarinho, "Al-Doped ZnO Thin Films by Sol-Gel Method," *Surface and Coatings Technology* 180 (2004): 659–662.
12. E. Hammarberg, A. Prodi-Schwab, and C. Feldmann, "Microwave-Assisted Polyol Synthesis of Aluminium- and Indium-Doped ZnO Nanocrystals," *Journal of Colloid and Interface Science* 334, no. 1 (2009): 29–36.
13. Z. Xu, H. Deng, Y. Li, Q. Guo, and Y. Li, "Characteristics of Al-Doped c-axis Orientation ZnO Thin Films Prepared by the Sol-Gel Method," *Materials Research Bulletin* 41, no. 2 (2006): 354–358.
14. K.-M. Lin and P. Tsai, "Growth Mechanism and Characterization of ZnO: Al Multi-Layered Thin Films by Sol-Gel Technique," *Thin Solid Films* 515, no. 24 (2007): 8601–8604.
15. J. Ederth, P. Heszler, A. Hultåker, G. Niklasson, and C. Granqvist, "Indium Tin Oxide Films Made From Nanoparticles: Models for the Optical and Electrical Properties," *Thin Solid Films* 445, no. 2 (2003): 199–206, in Proceedings of the 3rd International Symposium on Transparent Oxide Thin films for Electronics and Optics, [https://doi.org/10.1016/S0040-6090\(03\)01164-7](https://doi.org/10.1016/S0040-6090(03)01164-7).
16. R. Street, W. Wong, S. Ready, et al., "Jet Printing Flexible Displays," *Materials Today* 9, no. 4 (2006): 32–37.
17. D.-H. Lee, Y.-J. Chang, G. S. Herman, and C.-H. Chang, "A General Route to Printable High-Mobility Transparent Amorphous Oxide Semiconductors," *Advanced Materials* 19, no. 6 (2007): 843–847.

18. C. Rao, J. Rawlings, and D. Mayne, "Constrained State Estimation for Nonlinear Discrete-Time Systems: Stability and Moving Horizon Approximations," *IEEE Transactions on Automatic Control* 48, no. 2 (2003): 246–258.
19. P. Kühn, M. Diehl, T. Kraus, J. P. Schlöder, and H. G. Bock, "A Real-Time Algorithm for Moving Horizon State and Parameter Estimation," *Computers & Chemical Engineering* 35, no. 1 (2011): 71–83.
20. M. K. J. Dongmo and T. Meurer, "Moving Horizon Estimator Design for a Nonlinear Diffusion-Reaction System With Sensor Dynamics," *IFAC-PapersOnLine* 55, no. 20 (2022): 85–90.
21. G. Yang, M. K. Jiokeng Dongmo, S. Buchheiser, T. Meurer, and H. Nirschl, "Temperature-Driven Strategy for Engineering of Al-Doped ZnO Mesocrystals' Hierarchical Architecture," under review at *Industrial & Engineering Chemistry Research*; preprint at KITopen, <https://doi.org/10.5445/IR/1000180434>.
22. J. Ungerer, A.-K. Thurm, M. Meier, M. Klinge, G. Garnweitner, and H. Nirschl, "Development of a Growth Model for Aluminum-Doped Zinc Oxide Nanocrystal Synthesis via the Benzylamine Route," *Journal of Nanoparticle Research* 21, no. 5 (2019): 106.
23. J. Ungerer, A.-K. Thurm, G. Garnweitner, and H. Nirschl, "Formation of Aluminum-Doped Zinc Oxide Nanocrystals via the Benzylamine Route at Low Reaction Kinetics," *Chemical Engineering & Technology* 43, no. 5 (2020): 797–803.
24. D. Ramkrishna, *Population Balances: Theory and Applications to Particulate Systems in Engineering* (Academic Press, 2000).
25. B. J. McCoy and G. Madras, "Analytical Solution for a Population Balance Equation With Aggregation and Fragmentation," *Chemical Engineering Science* 58, no. 13 (2003): 3049–3051.
26. S. Kumar and D. Ramkrishna, "On the Solution of Population Balance Equations by Discretization—II. A Moving Pivot Technique," *Chemical Engineering Science* 51, no. 8 (1996): 1333–1342.
27. J. L. Proctor, S. L. Brunton, and J. N. Kutz, "Dynamic Mode Decomposition With Control," *SIAM Journal on Applied Dynamical Systems* 15, no. 1 (2016): 142–161.
28. D. A. Allan and J. B. Rawlings, "Moving Horizon Estimation," in *Handbook of Model Predictive Control* (Springer, 2019), 99–124.
29. J. B. Rawlings, "Moving Horizon Estimation," in *Encyclopedia of Systems and Control*, ed. J. Baillieul and T. Samad (Springer London, 2013), 1–7.
30. P. Jerono, A. Schaum, and T. Meurer, "Moment-Based Kalman Filter Design for Cell Population Balance Models in Batch Fermentation Processes," *IFAC-PapersOnLine* 54, no. 3 (2021): 19–24, in 16th IFAC Symposium on Advanced Control of Chemical Processes ADCHEM 2021. <https://doi.org/10.1016/j.ifacol.2021.08.212>.
31. P. Jerono, A. Schaum, and T. Meurer, "Observability Analysis and Robust Observer Design for a Continuous Yeast Culture," *Journal of Process Control* 104 (2021): 62–73.
32. P. Jerono, A. Schaum, and T. Meurer, "Continuous–Discrete Cell Mass Distribution Observer Design Using Impulsive Iss Lyapunov Functions," *IFAC-PapersOnLine* 55, no. 26 (2022): 20–25, in 4th IFAC Workshop on Control of Systems Governed by Partial Differential Equations CPDE 2022, <https://doi.org/10.1016/j.ifacol.2022.10.371>.
33. X. Li, S. Bo, X. Zhang, Y. Qin, and X. Yin, "Data-Driven Parallel Koopman Subsystem Modeling and Distributed Moving Horizon State Estimation for Large-Scale Nonlinear Processes," *AIChE Journal* (2023): e18326.
34. A. Pazy, *Semigroups of Linear Operators and Applications to Partial Differential Equations*, (Springer-Verlag, 1992).
35. M. K. Jiokeng Dongmo, Y. Guohui, H. Nirschl, and T. Meurer, "Moving Horizon Estimator Design for a Nanoparticle Synthesis Batch Process," *IFAC-PapersOnLine* 58, no. 14 (2024): 342–347, in 12th IFAC Symposium on Advanced Control of Chemical Processes ADCHEM 2024, <https://doi.org/10.1016/j.ifacol.2024.08.360>.
36. S. R. K. Perala and S. Kumar, "On the Two-Step Mechanism for Synthesis of Transition-Metal Nanoparticles," *Langmuir* 30, no. 42 (2014): 12703–12711, <https://dx.doi.org/10.1021/la503199m>.
37. E. Hansen, S. L. Brunton, and Z. Song, "Swarm Modeling With Dynamic Mode Decomposition," *IEEE Access* 10 (2022): 59508–59521, <https://dx.doi.org/10.1109/ACCESS.2022.3179414>.
38. M. Diehl, H. J. Ferreau, and N. Haverbeke, "Efficient Numerical Methods for Nonlinear MPC and Moving Horizon Estimation," in *Nonlinear Model Predictive Control* (Springer, 2009), 391–417.

Supporting Information

Additional supporting information can be found online in the Supporting Information section.

Supporting Information **Supporting file:** nano70044-sup-0001-SuppMat.docx.